

Dilute Magnetism and Spin-Orbital Percolation Effects in $\text{Sr}_2\text{Ir}_{1-x}\text{Rh}_x\text{O}_4$

J.P. Clancy,¹ A. Lupascu,¹ H. Gretarsson,¹ Z. Islam,² Y.F. Hu,³ D. Casa,² C.S. Nelson,⁴ S.C. LaMarra,⁴ G. Cao,⁵ and Young-June Kim¹

¹*Department of Physics, University of Toronto, Toronto, Ontario, M5S 1A7, Canada*

²*Advanced Photon Source, Argonne National Laboratory, Argonne, Illinois 60439, USA*

³*Canadian Light Source, Saskatoon, Saskatchewan, S7N 0X4, Canada*

⁴*National Synchrotron Light Source, Brookhaven National Laboratory, Upton, New York, 11973, USA*

⁵*Department of Physics and Astronomy, University of Kentucky, Lexington, Kentucky 40506, USA*

We have used a combination of resonant magnetic x-ray scattering (RMXS) and x-ray absorption spectroscopy (XAS) to investigate the properties of the doped spin-orbital Mott insulator $\text{Sr}_2\text{Ir}_{1-x}\text{Rh}_x\text{O}_4$ ($0.07 \leq x \leq 0.70$). We show that $\text{Sr}_2\text{Ir}_{1-x}\text{Rh}_x\text{O}_4$ represents a unique model system for the study of dilute magnetism in the presence of strong spin-orbit coupling, and provide evidence of a doping-induced change in magnetic structure and a suppression of magnetic order at $x_c \sim 0.17$. We demonstrate that Rh-doping introduces $\text{Rh}^{3+}/\text{Ir}^{5+}$ ions which effectively hole-dope this material. We propose that the magnetic phase diagram for this material can be understood in terms of a novel spin-orbital percolation picture.

PACS numbers: 75.25.-j, 78.70.Ck, 64.60.ah, 71.70.Ej

I. INTRODUCTION

The physics of iridium-based transition metal oxides has sparked significant interest due to the potential for exotic electronic and magnetic ground states driven by strong spin-orbit coupling (SOC). Due to the large atomic mass and broad electronic wavefunctions associated with 5d iridium, these materials tend to display strong relativistic SOC and crystal electric field (CEF) effects, but relatively weak electronic correlations (U). As a result, the properties of the 5d iridates are often dramatically different from those of their lighter 3d counterparts. The layered perovskite Sr_2IrO_4 has attracted particular attention as the first experimental realization of a $J_{eff} = 1/2$ spin-orbital Mott insulator^{1,2}. The magnetism in this compound arises from Ir^{4+} ions with a $5d^5$ electronic configuration. However, unlike conventional $S = 1/2$ magnetic moments, the $J_{eff} = 1/2$ moments of Sr_2IrO_4 possess mixed spin and orbital character, with magnetic exchange interactions that are strongly bond and lattice-dependent. For the bond geometry of Sr_2IrO_4 , these interactions can be described by an effectively isotropic Heisenberg Hamiltonian^{3,4}.

Sr_2IrO_4 has a tetragonal crystal structure (space group $I4_1/acd$, $a = 5.499 \text{ \AA}$, $c = 25.79 \text{ \AA}$) which consists of stacked layers of corner-sharing IrO_6 octahedra^{5,6}. This structure is a variant of the K_2NiF_4 structure shared by $\text{La}_{2-x}(\text{Ba},\text{Sr})_x\text{CuO}_4$ and Sr_2RuO_4 , differing only by a staggered $\sim 11^\circ$ rotation of IrO_6 octahedra about the c -axis. The structural and magnetic similarities between these compounds have led to natural associations with superconductivity, and recent theoretical proposals^{7,8} have spurred renewed interest in the properties of doped Sr_2IrO_4 . Although many forms of electron, hole, and isoelectronic doping have been experimentally tested to date⁹⁻²⁰, there is still much to learn

about the impact of doping on the spin-orbital Mott insulating ground state.

$\text{Sr}_2\text{Ir}_{1-x}\text{Rh}_x\text{O}_4$ represents an ideal candidate for experimental doping studies. Rh is situated directly above Ir in the periodic table, and Sr_2RhO_4 is a paramagnetic metal which is isostructural to Sr_2IrO_4 (with slightly reduced lattice parameters and an octahedral rotation of $\sim 9.7^\circ$)²¹⁻²³. Bulk characterization measurements on $\text{Sr}_2\text{Ir}_{1-x}\text{Rh}_x\text{O}_4$ have revealed a rich phase diagram with multiple electronic and magnetic transitions⁹. At low concentrations ($x \leq 0.16$), $\text{Sr}_2\text{Ir}_{1-x}\text{Rh}_x\text{O}_4$ is an antiferromagnetic insulator, while at higher dopings it becomes a paramagnetic metal/semiconductor ($0.16 \leq x \leq 0.24$), a frustrated magnetic insulator ($0.24 \leq x \leq 0.85$), and a paramagnetic correlated metal ($x \geq 0.85$). In the simplest scenario, one expects Rh-doping to result in an isoelectronic substitution of Ir^{4+} ($5d^5$) for Rh^{4+} ($4d^5$). Such a substitution would tune the SOC of the system from the strong 5d regime to the moderate 4d regime, but leave the band filling unaffected^{9,10}. However, it has also been proposed that the dopant ions may adopt a Rh^{3+} ($4d^6$) oxidation state, creating nearby Ir^{5+} ($5d^4$) ions in order to preserve charge neutrality¹¹⁻¹³. Such a substitution would not only tune SOC, but would also alter the band filling via hole-doping. A comparison of these two mechanisms is provided in Fig. 1(a). Rh^{4+} and Rh^{3+} substitution will also have very different effects on the magnetism of Sr_2IrO_4 , with Rh^{4+} doping resulting in an exchange of effective $S = 1/2$ moments, and Rh^{3+} doping introducing pairs of non-magnetic vacancies (Rh^{3+} and Ir^{5+} are both non-magnetic due to fully filled t_{2g} [Rh] and $J_{eff} = 3/2$ [Ir] electronic configurations).

In this article, we present complementary resonant magnetic x-ray scattering (RMXS) and x-ray absorption spectroscopy (XAS) measurements on single crystal sam-

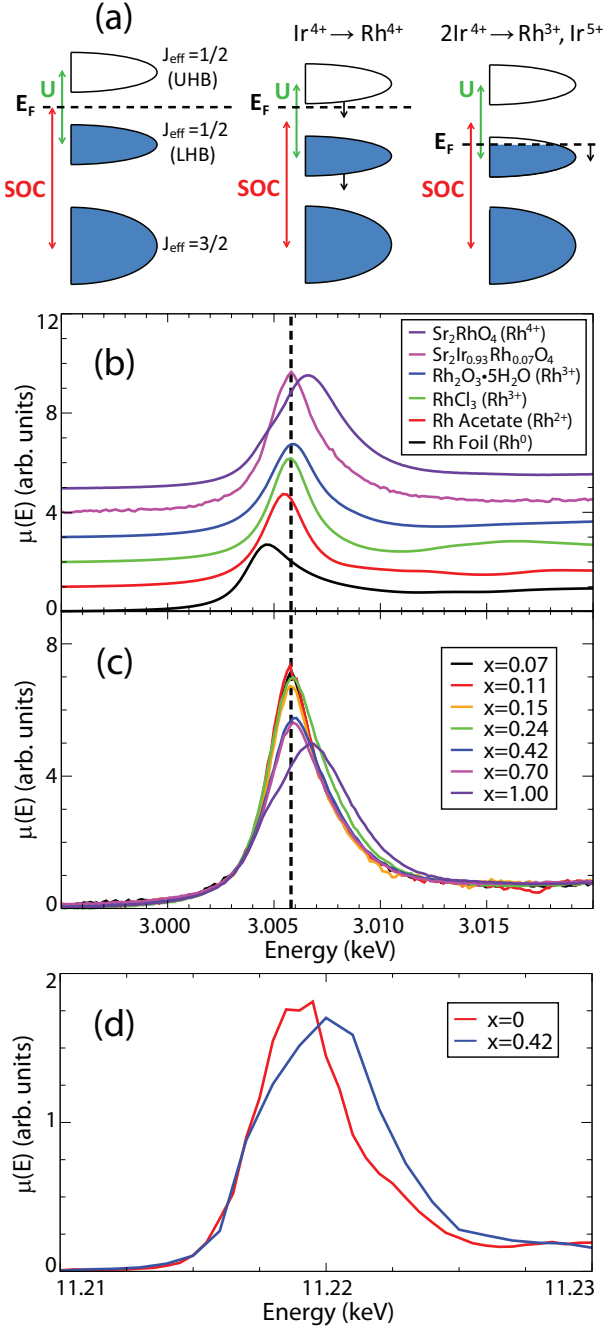


FIG. 1: (Color Online) (a) Potential effects of Rh-doping on the electronic band structure of Sr_2IrO_4 . Isoelectronic substitution of Rh^{4+} for Ir^{4+} is expected to tune the strength of the SOC, while substitution of Rh^{3+} is expected to reduce SOC and effectively hole-dope the system. (b) X-ray absorption spectra collected at the Rh L_3 -edge ($2p_{3/2} \rightarrow 4d$) for a series of Rh-based reference samples. The position of the white-line peak in $\text{Sr}_2\text{Ir}_{1-x}\text{Rh}_x\text{O}_4$ is consistent with a Rh^{3+} oxidation state. (c) Doping dependence of Rh L_3 -edge absorption spectra for $\text{Sr}_2\text{Ir}_{1-x}\text{Rh}_x\text{O}_4$. The position of the white-line feature remains unchanged for $0.07 \leq x \leq 0.70$. (d) X-ray absorption spectra collected at the Ir L_3 -edge ($2p_{3/2} \rightarrow 5d$) for samples with $x = 0$ and $x = 0.42$. The positive chemical shift and the broadening of the white-line feature are consistent with a mixed population of Ir^{4+} and Ir^{5+} ions introduced by doping.

ples of $\text{Sr}_2\text{Ir}_{1-x}\text{Rh}_x\text{O}_4$ ($0.07 \leq x \leq 0.70$). Our results clearly demonstrate that $\text{Sr}_2\text{Ir}_{1-x}\text{Rh}_x\text{O}_4$ must be considered as a hole-doped and magnetically diluted system. We show that Rh-doping results in a change of magnetic structure, a rapid decrease in magnetic transition temperatures, and a suppression of magnetic order at $x_c \sim 0.17$. In contrast to diluted La_2CuO_4 , we show that the magnetic phase diagram of $\text{Sr}_2\text{Ir}_{1-x}\text{Rh}_x\text{O}_4$ cannot be described by a conventional spin-only percolation picture. We propose that this discrepancy may reflect the importance of both spin and orbital percolation effects, which arise due to the strong SOC inherent to this system.

II. EXPERIMENTAL DETAILS

Single crystal samples of $\text{Sr}_2\text{Ir}_{1-x}\text{Rh}_x\text{O}_4$ ($0 \leq x \leq 1.0$) were prepared using self-flux techniques, as described elsewhere^{9,24}. The samples used in this experiment had typical dimensions of $\sim 2.0 \times 1.0 \times 0.1 \text{ mm}^3$. Detailed magnetization, resistivity, and specific heat measurements on these samples have previously been reported by Qi et al⁹. The Rh content of each sample was determined by energy dispersive x-ray (EDX) spectroscopy using a combined Hitachi/Oxford SwiftED 3000 unit. Crystal quality was assessed by x-ray rocking scans, which revealed sample mosaicities of $\sim 0.01^\circ$ to 0.15° full-width at half-maximum (FWHM). In particular, the three samples which lie within the magnetically-ordered region of the phase diagram ($x = 0.07, 0.11$, and 0.15) all displayed FWHM of 0.02° or better.

X-ray absorption spectroscopy measurements were performed using the Soft X-ray Microcharacterization Beamline (SXRMB) at the Canadian Light Source (CLS) and Beamline 9-ID-B at the Advanced Photon Source (APS) at Argonne National Laboratory. Measurements on SXRMB were carried out at the Rh L_3 ($2p_{3/2} \rightarrow 4d$) and L_2 ($2p_{1/2} \rightarrow 4d$) absorption edges, which occur at energies of 3.004 keV and 3.146 keV respectively. Data was collected using Total Electron Yield (TEY) and Fluorescence Yield (FY) detection modes, and energy calibration was verified by a comparison of Ar K-edge features observed at $E = 3.206 \text{ keV}$. Measurements on 9-ID-B were carried out at the Ir L_3 absorption edge ($2p_{3/2} \rightarrow 5d$, $E = 11.215 \text{ keV}$), using Partial Fluorescence Yield (PFY) detection mode. PFY-XAS is a form of resonant x-ray emission spectroscopy, which involves tuning the incident energy to the Ir L_3 -edge, and monitoring the intensity of the Ir $L\alpha_2$ emission line ($3d_{3/2} \rightarrow 2p_{3/2}$, $E = 9.099 \text{ keV}$) as a function of energy. By suppressing the spectral broadening due to $2p$ core-hole lifetime effects, PFY-XAS can provide a significant improvement in experimental energy resolution^{25,26}. These measurements were carried out using a double-bounce Si-(1,1,1) primary monochromator, a channel-cut Si-(3,3,3) secondary monochromator, and a spherical (1m radius)

diced Ge-(3,3,7) analyzer crystal to obtain an instrumental energy resolution of 225 meV (FWHM). Measurements were collected using horizontal scattering geometry, with a scattering angle close to $2\theta = 90^\circ$.

Resonant magnetic x-ray scattering measurements were performed using Beamline 6-ID-B at the APS. Measurements were carried out at the Ir L_3 ($2p_{3/2} \rightarrow 5d$) and L_2 ($2p_{1/2} \rightarrow 5d$) absorption edges, which occur at energies of 11.215 keV and 12.824 keV respectively. Samples were mounted in a closed-cycle cryostat with a base temperature of $T = 6$ K. Measurements were performed in vertical scattering geometry, with the polarization of the incident beam perpendicular to the scattering plane defined by \mathbf{k}_i and \mathbf{k}_f (i.e. a σ -polarized beam). The polarization of the scattered beam was analyzed using the (0,0,8) and (0,0,10) reflections from a pyrolytic graphite (PG) analyzer crystal. These reflections correspond to analyzer scattering angles of $2\theta_p = 82.33^\circ$ at the Ir L_3 -edge and $2\theta_p = 92.04^\circ$ at the Ir L_2 -edge, respectively. In this configuration, the scattering term with a rotated polarization vector (i.e. σ - π) is magnetic in origin, while the term with an unrotated polarization vector (i.e. σ - σ) is due to charge scattering. The intensity of the magnetic scattering contribution is proportional to $(\mathbf{k}_f \cdot \mathbf{M})^2$ [Ref. 27].

High-resolution non-resonant x-ray diffraction measurements were performed using Beamline X21 at the National Synchrotron Light Source (NSLS) at Brookhaven National Laboratory. Measurements were carried out in vertical scattering geometry, using x-rays with an incident energy of 11.000 keV. A Ge-(1,1,1) analyzer was used to improve angular resolution and reduce experimental background.

III. EXPERIMENTAL RESULTS

A. Ionic Composition of $\text{Sr}_2\text{Ir}_{1-x}\text{Rh}_x\text{O}_4$

To investigate the role of the Rh dopant ions in $\text{Sr}_2\text{Ir}_{1-x}\text{Rh}_x\text{O}_4$ we performed x-ray absorption spectroscopy (XAS) measurements at the Rh L_3 -edge. The position of the sharp “white-line” peak at the absorption edge is very sensitive to oxidation state, and displays a chemical shift which is proportional to the ionic charge. Fig. 1(b) shows representative x-ray absorption spectra for a series of Rh-based reference samples, with oxidation states ranging from 0 to 4+. The white-line peak for $\text{Sr}_2\text{Ir}_{0.93}\text{Rh}_{0.07}\text{O}_4$ clearly coincides with the Rh^{3+} reference samples, and is shifted by ~ -1.4 eV with respect to Rh^{4+} . The doping dependence of the absorption spectra (Fig. 1(c)) indicates that the position of the white-line peak remains fixed for $x = 0.07$ to $x = 0.70$.

By performing similar XAS measurements at the Ir L_3 -edge (Fig. 1(d)) we can also characterize the doping dependence of the Ir oxidation state. These measure-

TABLE I: Doping dependence of Rh L_3 -edge XAS parameters for $\text{Sr}_2\text{Ir}_{1-x}\text{Rh}_x\text{O}_4$. The position and the width (FWHM) of the Rh L_3 -edge white-line feature have been obtained from fits performed using a simple two component (Lorentzian + Arctangent) fit function.

Rh Concentration	Peak Position (eV)	Peak Width (eV)
$x = 0.07$	3005.8 ± 0.1	3.2 ± 0.1
$x = 0.11$	3005.8 ± 0.1	3.1 ± 0.1
$x = 0.15$	3005.8 ± 0.1	3.3 ± 0.1
$x = 0.24$	3005.9 ± 0.1	3.4 ± 0.1
$x = 0.42$	3005.9 ± 0.1	4.1 ± 0.1
$x = 0.70$	3005.9 ± 0.1	3.9 ± 0.1
$x = 1.00$	3007.2 ± 0.1	3.9 ± 0.2

ments reveal a broadening of the Ir L_3 -edge white-line peak and a positive shift in spectral weight with increasing Rh concentration. Both of these features are consistent with a mixed population of Ir^{4+} and Ir^{5+} ions introduced by doping. It should be noted that the doping dependence of the Ir L_3 -edge absorption spectra is difficult to observe with conventional XAS methods due to the effect of core-hole lifetime broadening, which is more than twice as large for Ir (5.3 eV) as it is for Rh (2.1 eV)²⁸. It is only by utilizing the PFY-XAS technique, which suppresses such core-hole lifetime effects, that we can resolve these features in the present study.

The combination of Rh and Ir XAS results allow us to draw four main conclusions: (1) The Rh dopant ions in $\text{Sr}_2\text{Ir}_{1-x}\text{Rh}_x\text{O}_4$ adopt a 3+ rather than 4+ oxidation state. (2) This oxidation state persists across almost the entire Rh-doped phase diagram. (3) The electronic effect of Rh-doping is to tune band-filling via hole-doping. (4) The magnetic effect of Rh-doping is to introduce quenched non-magnetic vacancies (2 per dopant ion).

We must emphasize that while the $\text{Rh}^{3+}/\text{Ir}^{5+}$ picture will accurately describe $\text{Sr}_2\text{Ir}_{1-x}\text{Rh}_x\text{O}_4$ at low dopings, and within the percolation regime that our RMXS measurements will focus on (i.e. for $0 \leq x \leq 0.24$), at higher dopings this picture must be modified. The complication arises from the fact that once the concentration of Rh reaches $x = 0.50$ there will no longer be enough potential Ir^{5+} ions available to balance the electronic charge. As a result, while the lower dopings will be dominated by Rh^{3+} ions, the higher dopings must contain some mixture of 3+ and 4+ oxidation states. This scenario appears to be consistent with the XAS fit parameters provided in Table I. Although the position of the Rh L_3 edge white-line does not change between $x = 0.07$ and $x = 0.70$, the width of the white-line peak becomes significantly broader for $x = 0.42$ and $x = 0.70$. This broadening is consistent with the development of a high-energy shoulder on the white-line peak, as one would expect for an increasing, but still minority, population of Rh^{4+} ions.

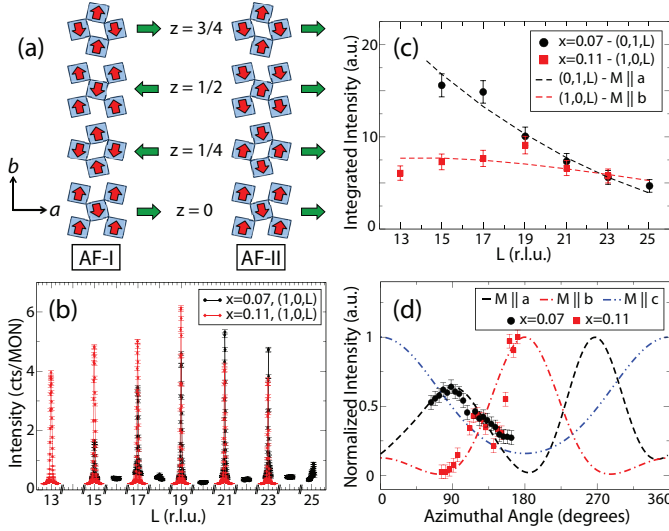


FIG. 2: (Color Online) (a) Canted antiferromagnetic ground states of $\text{Sr}_2\text{Ir}_{1-x}\text{Rh}_x\text{O}_4$. The AF-I spin configuration is observed for $x = 0$, while the AF-II configuration is observed for $0.07 \leq x \leq 0.15$. The net ferromagnetic moment in each Ir-O layer is denoted by a green arrow. (b) Observed magnetic Bragg peaks in $\text{Sr}_2\text{Ir}_{1-x}\text{Rh}_x\text{O}_4$ for $x = 0.07$ and $x = 0.11$. (c) Theoretical modelling of the magnetic structure factor is consistent with a canted antiferromagnetic structure (AF-II) which has a magnetic easy-axis in the ab -plane. (d) The azimuthal dependence of the $(0,1,21)$ magnetic peak intensity confirms that the orientation of the moments is along the a and b -axes. The data in panels (b)-(d) was collected at $T = 7$ K and $E_i = 11.217$ keV, using σ - π polarization analysis.

B. Magnetic Structure of $\text{Sr}_2\text{Ir}_{1-x}\text{Rh}_x\text{O}_4$

The impact of Rh-doping on magnetic structure was investigated using resonant magnetic x-ray scattering (RMXS). The magnetic ground state of pure Sr_2IrO_4 is known to be a canted ab -plane antiferromagnet in which magnetic moments follow the rotations of IrO_6 octahedra^{2,29}. This structure, AF-I, is illustrated in Fig. 2(a). The magnetic structure of $\text{Sr}_2\text{Ir}_{1-x}\text{Rh}_x\text{O}_4$ was determined using three different elements from the RMXS data: (1) the magnetic selection rule, (2) the magnetic structure factor, and (3) the azimuthal dependence of the magnetic Bragg peaks.

The simplest of these elements is the magnetic selection rule, which is illustrated in Fig. 2(b). This panel shows the characteristic magnetic Bragg peaks which develop in $\text{Sr}_2\text{Ir}_{1-x}\text{Rh}_x\text{O}_4$ for dopings of $x = 0.07$ and $x = 0.11$. Note that on the basis of this selection rule alone, one can immediately identify that a doping-induced magnetic phase transition takes place between $x = 0$ and $x = 0.07$. The AF-I magnetic structure which develops in undoped Sr_2IrO_4 ($x = 0$) gives rise to magnetic Bragg peaks at $(1,0,L)/(0,1,L)$ wave vectors for $L = \text{even}$, and $(0,0,L)$ wave vectors for $L = \text{odd}$. A single AF-I domain pro-

duces magnetic peaks at $(1,0,4n+2)$ and $(0,1,4n)$ wave vectors for all integer n . However, given the tetragonal crystal structure of Sr_2IrO_4 , it is natural for a two-domain magnetic structure to develop, with the second domain giving rise to peaks at $(1,0,4n)$ and $(0,1,4n+2)$. This selection rule is clearly inconsistent with the data in Fig. 2(b), allowing us to rule out the possibility of an AF-I spin configuration for $x = 0.07$ and $x = 0.11$.

The magnetic Bragg peaks observed in $\text{Sr}_2\text{Ir}_{1-x}\text{Rh}_x\text{O}_4$ ($0.07 \leq x \leq 0.15$) appear at $(1,0,L)/(0,1,L)$ wave vectors for $L = \text{odd}$. Scans along other high symmetry directions in reciprocal space, such as $[0,0,L]$, $[1,1,L]$, $[1/2,1/2,L]$, and $[1/2,0,L]$, reveal no evidence of additional magnetic peaks, either at commensurate or incommensurate wave vectors. These magnetic peaks are consistent with a $\mathbf{k} = (0,0,0)$ magnetic propagation vector. Following a similar approach to Calder et al¹⁴, we used representational analysis to identify potential magnetic structures for $\text{Sr}_2\text{Ir}_{1-x}\text{Rh}_x\text{O}_4$. This analysis was performed using the SARAh Representational Analysis software package³⁰. For a crystal structure with $I4_1/acd$ symmetry and magnetic moments located on the Ir 8a site, there are only six irreducible representations consistent with a propagation vector of $\mathbf{k} = (0,0,0)$: Γ_1 , Γ_3 , Γ_6 , Γ_8 , Γ_9 , and Γ_{10} . Two of these representations can immediately be discarded as they fail to reproduce the observed magnetic Bragg peaks - Γ_3 (which describes a magnetic structure with ferromagnetic in-plane coupling, ferromagnetic out-of-plane coupling, and moments oriented along the c -axis), and Γ_6 (which describes a magnetic structure with ferromagnetic in-plane coupling, antiferromagnetic out-of-plane coupling, and moments oriented along the c -axis). The four remaining irreducible representations (Γ_1 , Γ_8 , Γ_9 , and Γ_{10}) are all characterized by antiferromagnetic in-plane coupling, and antiferromagnetic out-of-plane coupling. The chief distinction between these representations is the choice of magnetic easy axis. Γ_1 and Γ_8 describe magnetic structures with moments oriented along the c -axis (as in the doping-induced state observed in $\text{Sr}_2\text{Ir}_{0.9}\text{Mn}_{0.1}\text{O}_4$ [Ref. 14], while Γ_9 and Γ_{10} describe structures with moments in the ab -plane (as in the field-induced state of Sr_2IrO_4 [Ref. 2]). The magnetic structure corresponding to Γ_9 and Γ_{10} , which we will label AF-II, is illustrated in Fig. 2(a).

In order to distinguish between these possible structures, we can model both the magnetic structure factor and the azimuthal dependence of the magnetic Bragg peaks. These quantities are both sensitive to the orientation of the magnetic moments, and can be calculated using the FDMNES software package³¹. For simplicity, we have employed a single-domain model for these calculations, which assumes one dominant magnetic domain. The integrated intensity of the magnetic Bragg peaks (obtained from θ or rocking scans) is plotted as a function of L in Fig. 2(c). These measurements were performed with the sample aligned such that the $[1,1,0]$ and

[0,0,1] directions are coincident with the vertical scattering plane. In this orientation, there will be non-zero magnetic scattering contributions from moments aligned along the a , b , or c -axes. However, a satisfactory fit to the magnetic structure factor can only be obtained for moments oriented within the ab -plane - either along the a -axis ($x = 0.07$) or along the b -axis ($x = 0.11$). Note that because the crystal structure of $\text{Sr}_2\text{Ir}_{1-x}\text{Rh}_x\text{O}_4$ has tetragonal symmetry, there is no physical distinction between these two axes. Hence the apparent 90° rotation of moment direction between $x = 0.07$ and $x = 0.11$ is simply due to a spontaneous choice of $[1,0,0]/[0,1,0]$ orientation adopted by the dominant grain upon cooling through T_{N1} .

The azimuthal dependence of the magnetic Bragg peaks in $\text{Sr}_2\text{Ir}_{1-x}\text{Rh}_x\text{O}_4$ (Fig. 2(d)) is also consistent with magnetic moments oriented in the ab -plane. Here $\phi = 0^\circ$ has been defined as the sample orientation for which $[0,1,0]$ is coincident with the vertical scattering plane defined by \mathbf{k}_i and \mathbf{k}_f . The modeling of the azimuthal dependence indicates that the magnetic easy axis is along the a -axis for $x = 0.07$, and along the b -axis for $x = 0.11$, in full agreement with the results of the structure factor calculation. In particular, two qualitative features of the azimuthal dependence - the 180° oscillation period and the vanishing of magnetic intensity at specific angles - cannot be reproduced by a magnetic structure which has a c -axis spin configuration.

The results of our magnetic structure analysis indicate that: (1) $\text{Sr}_2\text{Ir}_x\text{Rh}_{1-x}\text{O}_4$ undergoes a doping-induced magnetic phase transition at $x \leq 0.07$, (2) the magnetic ground state of Sr_2IrO_4 is very sensitive to a variety of external perturbations, and (3) the effects of quenched magnetic (Mn) and non-magnetic (Rh) impurities are significantly different. It should be noted that a full magnetic structure factor and azimuthal dependence measurement was not completed for the $x = 0.15$ sample. We have attributed the same AF-II magnetic structure to this compound based purely on the magnetic selection rule. As in the case of the $x = 0.07$ and $x = 0.11$ compounds, this sample displays magnetic Bragg peaks at $(1,0,L)$ and $(0,1,L)$ wave vectors for $L = \text{odd}$, but not for $L = \text{even}$. Additional follow-up measurements would be required for an unambiguous determination of the magnetic structure and moment direction for this doping.

C. Magnetic Order Parameter and Correlation Lengths in $\text{Sr}_2\text{Ir}_{1-x}\text{Rh}_x\text{O}_4$

The temperature dependence of the magnetic peak intensity (Fig. 3) provides a direct measure of the antiferromagnetic order parameter ($I \sim M^2$). The magnetic peak intensity closely tracks the bulk magnetization⁹, with T_{N1} marking the appearance of magnetic Bragg

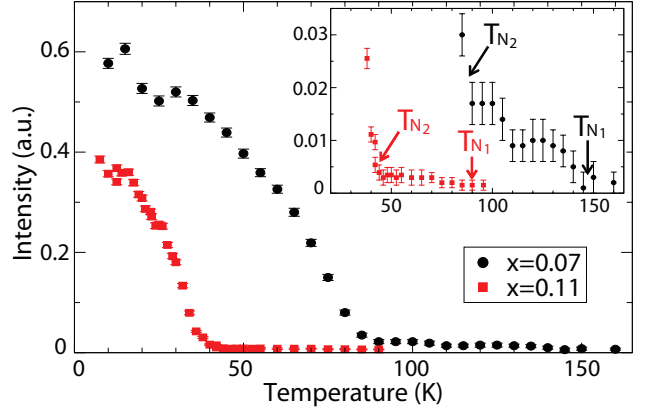


FIG. 3: (Color Online) Temperature dependence of the (0,1,21) magnetic Bragg peak measured at the Ir L_3 -edge. The magnetic peak intensity is significantly reduced above T_{N2} , but remains finite up to T_{N1} (as shown in the inset). Magnetic peak intensities from the $x = 0.07$ and $x = 0.11$ samples have been normalized with respect to each other, using the intensities of nearby structural Bragg peaks for reference. Data in this panel was collected at $E_i = 11.217$ keV, using σ - π polarization analysis.

peaks and a net ferromagnetic moment, and T_{N2} marking a dramatic increase in peak intensity and a magnetization kink. Although the magnetic peaks persist between T_{N1} and T_{N2} , they display a broadened lineshape which is indicative of finite magnetic correlation lengths. By combining our RMXS measurements with previously reported magnetization data⁹, we can construct the magnetic phase diagram provided in Fig. 4(a).

These results suggest that the magnetic phase diagram of $\text{Sr}_2\text{Ir}_{1-x}\text{Rh}_x\text{O}_4$ is characterized by two distinct regions of AF-II magnetic order; a long-range-ordered (LRO) phase below T_{N2} , and a short-range-ordered (SRO) phase between T_{N1} and T_{N2} . The change in magnetic correlation lengths at T_{N2} is reflected in the width of the magnetic Bragg peaks, as shown in Fig. 5. The magnetic peaks within the SRO phase are significantly weaker than those observed in the LRO phase, and appear to be broader along both the in-plane ($[H,0,0]$ and $[0,K,0]$) and out-of-plane ($[0,0,L]$) directions. The experimentally measured peak width (expressed as the FWHM, Γ_{obs}) represents a convolution of the intrinsic peak width (Γ_{int}) and the instrumental resolution function (Γ_{res}). In this case, an experimental resolution function was determined by measuring the lineshape of a nearby structural Bragg peak. For the L-scans provided in Fig. 5, the width of the experimental resolution function was $\Gamma_{res} \sim 0.0066$ r.l.u. The magnetic correlation length (ξ) is inversely proportional to the intrinsic peak width through the relation: $\xi = [(2\pi/d)(\Gamma_{int}/2)]^{-1}$. This allows us to determine the average magnetic correlation lengths within the SRO phase, which are found to be $\xi_{ab} \sim 1500$ Å ($x = 0.07$) and 1400 Å ($x = 0.11$)

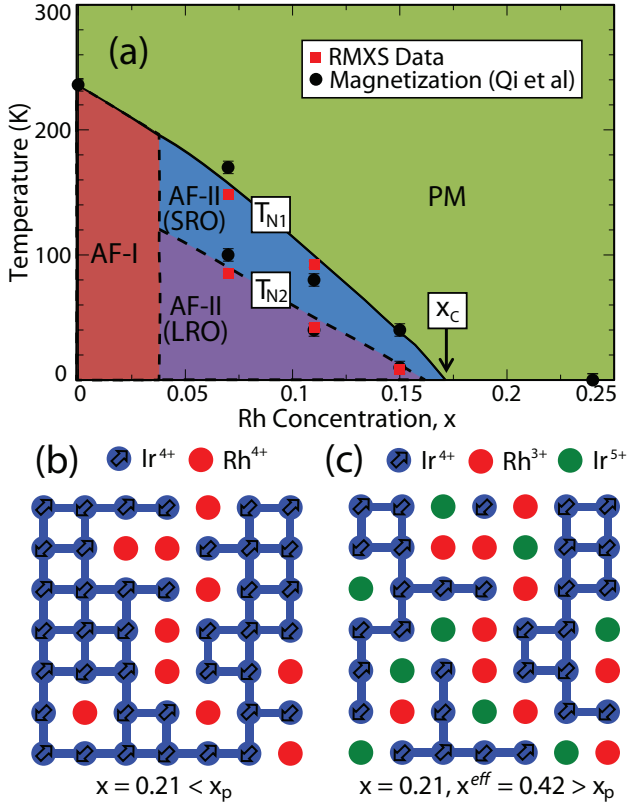


FIG. 4: (Color Online) (a) The magnetic phase diagram of $\text{Sr}_2\text{Ir}_{1-x}\text{Rh}_x\text{O}_4$, as constructed from RMXS and previously reported magnetization results⁹. The disappearance of magnetic order at $x_c \sim 0.17$ can be understood in terms of a spin-orbital percolation picture. (b) If Ir^{4+} is substituted for Rh^{4+} , then each dopant ion introduces one magnetic/orbital defect (replacing a $J_{eff} = 1/2$ Ir moment with a $S = 1/2$ Rh moment). In this scenario, a doping of $x = 0.21$ falls well below the spin-only percolation threshold of $x_p = 0.407$. (c) Alternatively, if Ir^{4+} is substituted for Rh^{3+} , then each dopant ion introduces two magnetic/orbital defects (one from the Rh^{3+} [$S = 0$], and one from its Ir^{5+} [$J_{eff} = 0$] ionic counterpart). In this scenario, the same doping ($x = 0.21$) is now sufficient to exceed the percolation threshold and destroy magnetic order. The discrepancy between $2x_c$ and x_p reflects the importance of orbital percolation effects, which arise due to the strong SOC of this system.

in-plane, and $\xi_c \sim 1000$ Å ($x = 0.07$) and 800 Å ($x = 0.11$) out-of-plane. Note that in both of these samples the average magnetic correlation length is substantially longer than the average distance between Rh dopant ions (~ 95 Å and 60 Å, respectively).

To summarize, the magnetic phase diagram of $\text{Sr}_2\text{Ir}_{1-x}\text{Rh}_x\text{O}_4$ is distinguished by three major features: (1) the disappearance of magnetic order at a critical doping of $x_c \sim 0.17$, (2) a doping-induced change in magnetic structure between $x = 0$ and $x = 0.07$, and (3) a thermally-driven transition between long-range (LRO)

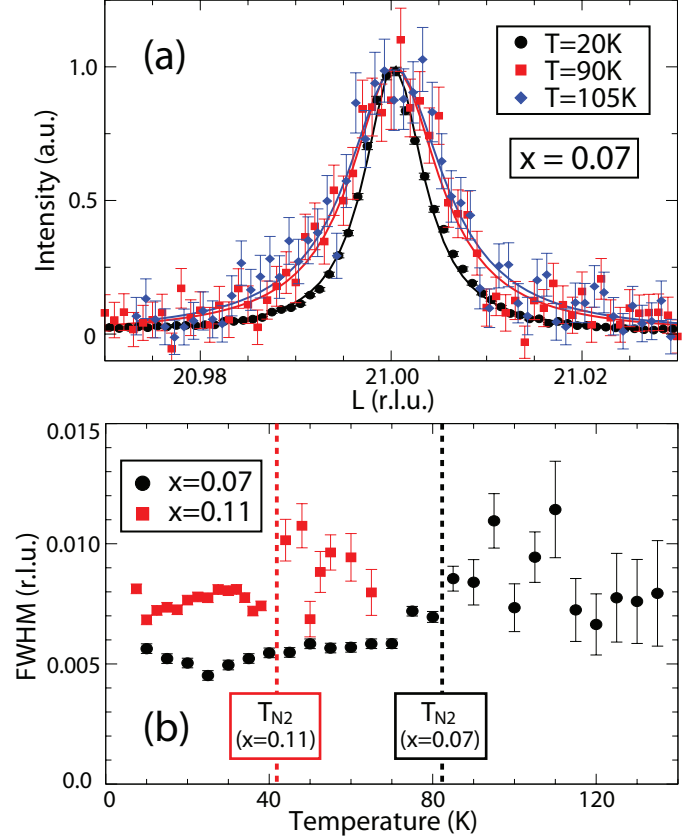


FIG. 5: (Color Online) Magnetic correlation lengths in $\text{Sr}_2\text{Ir}_{1-x}\text{Rh}_x\text{O}_4$. (a) Reciprocal space scans through the (0,1,21) magnetic Bragg peak in $\text{Sr}_2\text{Ir}_{0.93}\text{Rh}_{0.07}\text{O}_4$ at temperatures below ($T = 20$ K) and above ($T = 90, 105$ K) the magnetic transition at T_{N2} . (b) Temperature dependence of the magnetic peak width along $[0,0,L]$ for samples with $x = 0.07$ and $x = 0.11$. The FWHM in this panel represents the intrinsic peak width, determined from resolution-convoluted fits. The broadening of the magnetic peak widths above T_{N2} indicates the presence of finite magnetic correlation lengths between T_{N1} and T_{N2} . The correlation lengths within this phase range from 800 to 1000 Å.

and short-range (SRO) magnetic order at T_{N2} .

D. Robustness of the $J_{eff} = 1/2$ Ground State

The RMXS data also allows us to address the question of how Rh-doping affects the $J_{eff} = 1/2$ character of Sr_2IrO_4 . In previous work^{2,14,32-35}, the $J_{eff} = 1/2$ ground state has been identified on the basis of an anomalously large L_3/L_2 magnetic intensity ratio, which arises due to the selection rules and transition matrix elements associated with the L_2 ($2p_{1/2} \rightarrow 5d_{3/2}$) and L_3 ($2p_{3/2} \rightarrow 5d_{3/2}, 5d_{5/2}$) RMXS processes. The energy dependence of the (0,1,21) magnetic Bragg peak in $\text{Sr}_2\text{Ir}_{1-x}\text{Rh}_x\text{O}_4$ is provided in Fig. 6. Note that

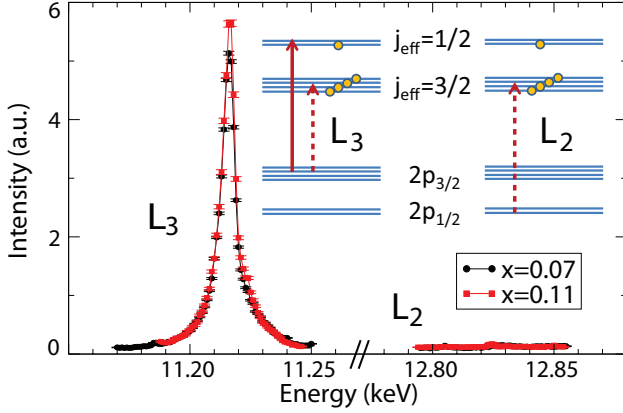


FIG. 6: (Color Online) Energy dependence of the (0,1,21) magnetic Bragg peak measured at the Ir L_3 ($E = 11.215$ keV) and L_2 ($E = 12.824$ keV) absorption edges. The large L_3/L_2 intensity ratio associated with the $J_{eff} = 1/2$ ground state remains unaffected by Rh concentrations up to $x = 0.11$. All data presented in this figure was collected at $T = 7$ K.

extremely large L_3/L_2 intensity ratios are observed for both the $x = 0.07$ and $x = 0.11$ samples. In fact, no magnetic Bragg peaks could be detected at the L_2 edge for either sample, indicating that $I(L_3)/I(L_2) > 200$. A similar result has also been reported for $\text{Sr}_2\text{Ir}_{0.9}\text{Mn}_{0.1}\text{O}_4$ [Ref. 14], suggesting that the $J_{eff} = 1/2$ character of Sr_2IrO_4 is very robust against doping in general. This persistence of strong J_{eff} character implies that the electronic transition at $x \sim 0.16$ is not driven by the tuning of SOC effects, but rather by a combination of hole-doping and/or doping-induced structural changes⁹.

It should be noted that the interpretation of the L_3/L_2 magnetic intensity ratio has recently been questioned by Chapon and Lovesey³⁶ and Moretti Sala et al³⁷. In particular, it has been suggested that the magnetic intensity at the L_2 -edge may vanish if Ir^{4+} magnetic moments are aligned within the ab -plane, regardless of the splitting of the t_{2g} levels. This point is relevant to both Sr_2IrO_4 and $\text{Sr}_2\text{Ir}_{1-x}\text{Rh}_x\text{O}_4$, as both systems adopt canted ab -plane antiferromagnetic ground states below T_N . However, in the case of $\text{Sr}_2\text{Ir}_{0.90}\text{Mn}_{0.10}\text{O}_4$, which displays a collinear c -axis antiferromagnetic structure¹⁴, this objection does not apply. In addition, Mn-doping represents an even stronger perturbation to magnetism ($J_{eff} = 1/2 \rightarrow S = 3/2$) and SOC ($5d \rightarrow 3d$) than Rh-doping. Although the signatures of the $J_{eff} = 1/2$ state in $\text{Sr}_2\text{Ir}_{1-x}\text{Rh}_x\text{O}_4$ may still require further investigation, the analogy with $\text{Sr}_2\text{Ir}_{1-x}\text{Mn}_x\text{O}_4$ suggests that, at least on a qualitative level, these conclusions will still hold true.

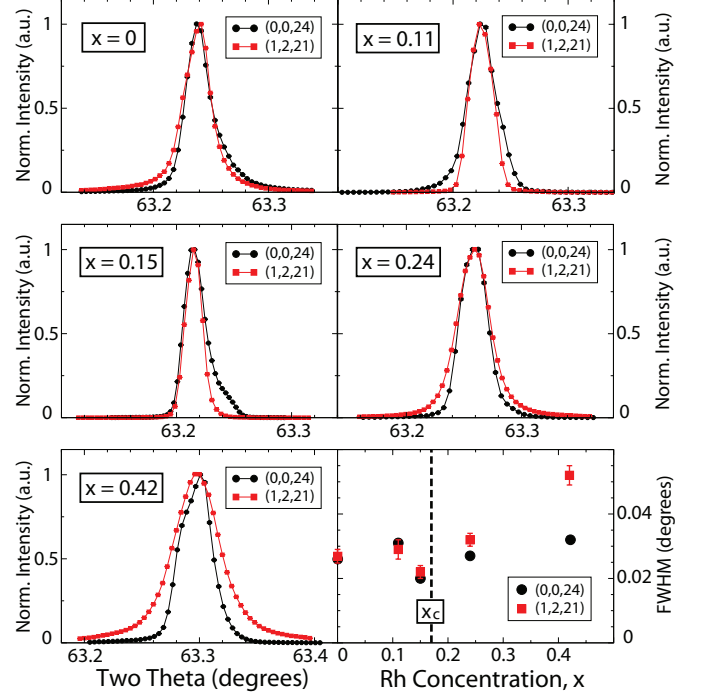


FIG. 7: (Color Online) High-resolution x-ray diffraction measurements on $\text{Sr}_2\text{Ir}_{1-x}\text{Rh}_x\text{O}_4$. This figure presents a collection of longitudinal (θ - 2θ) scans through the (0,0,24) structural Bragg peak and (1,2,21) superlattice Bragg peak for samples with $x = 0, 0.11, 0.15, 0.24$, and 0.42 . For illustrative purposes, scans through the (0,0,24) peak ($2\theta \sim 61.8^\circ$) have been horizontally translated and centered. The (1,2,21) superlattice peak arises due to correlated rotations of the $\text{IrO}_6/\text{RhO}_6$ octahedra. The width of the superlattice peak is approximately equal to that of the Bragg peak for $0 \leq x \leq 0.24$, indicating that the $\text{IrO}_6/\text{RhO}_6$ rotations are well-correlated at low dopings. By $x = 0.42$ the superlattice peak is considerably broader, indicating significant rotational disorder at higher dopings. All data presented in this figure was collected at $T = 300$ K.

E. Octahedral Rotations and Structural Disorder in $\text{Sr}_2\text{Ir}_{1-x}\text{Rh}_x\text{O}_4$

The rotations of IrO_6 octahedra are known to play an important role in shaping the physics of Sr_2IrO_4 . These rotations break the inversion symmetry between nearest-neighbor Ir ions, giving rise to an antisymmetric Dzyaloshinskii-Moriya interaction³. In addition, the orientation of the ordered moments in Sr_2IrO_4 appears to be strongly coupled to the octahedral rotations, with the canted antiferromagnetic ground state displaying a spin-canting angle of $\sim 8^\circ$ [Refs. 2, 24]. Given the difference in rotation angles between Sr_2IrO_4 ($\sim 11^\circ$) and Sr_2RhO_4 ($\sim 9.7^\circ$), the disorder of $\text{IrO}_6/\text{RhO}_6$ octahedral rotations has been proposed as one possible explanation for the suppression of magnetic order in $\text{Sr}_2\text{Ir}_{1-x}\text{Rh}_x\text{O}_4$ [Ref. 9].

In order to investigate how the $\text{IrO}_6/\text{RhO}_6$ octahedral rotations in $\text{Sr}_2\text{Ir}_{1-x}\text{Rh}_x\text{O}_4$ evolve as a function of doping, we performed a series of high-resolution non-resonant x-ray diffraction measurements. Fig. 7 provides a comparison of longitudinal (θ - 2θ) scans taken through the (0,0,24) structural Bragg peak and the (1,2,21) superlattice Bragg peak for samples with $x = 0, 0.11, 0.15, 0.24$, and 0.42 . The (1,2,21) superlattice peak arises due to the correlated rotations of the IrO_6 octahedra, and it is one of the distinguishing characteristics of the I_{41}/acd spacegroup^{5,6}. In the absence of correlated octahedral rotations, the superlattice peaks at (1,2,L)/(2,1,L), $L = \text{odd}$, disappear and Sr_2IrO_4 can be described by an I_4/mmm spacegroup, with a unit cell reduced by $\sqrt{2} \times \sqrt{2}$ in the ab -plane and halved along the c -axis. As a result, the width of the (1,2,21) superlattice peak provides a window into the correlation lengths associated with these octahedral rotations. For dopings of $x = 0$ to $x = 0.24$ the width of the superlattice peak is essentially the same as that of the structural Bragg peak, implying that the correlation lengths are long-ranged and the octahedral rotations are well-ordered. At higher dopings ($x = 0.42$), the superlattice peak becomes significantly broader than the Bragg peak, indicating reduced octahedral correlation lengths ($\xi_{rot} \sim 500 \text{ \AA}$) and increased rotational disorder. This suggests that while rotational disorder may play an important role in $\text{Sr}_2\text{Ir}_{1-x}\text{Rh}_x\text{O}_4$ at higher dopings ($x \geq 0.42$), it is not a significant effect at lower dopings ($x \leq 0.24$), and is unlikely to drive the suppression of magnetic order at x_c .

IV. DISCUSSION AND CONCLUSIONS

It is very interesting to consider the mechanism responsible for the disappearance of magnetic order at $x_c \sim 0.17$. We have already touched upon two potential mechanisms for this transition in the preceding sections. From the lack of doping-dependence associated with the L_3/L_2 magnetic intensity ratio (Section III.D), we infer that this magnetic transition is not the result of spin-orbit tuning. Similarly, although it is possible for magnetic order to be disrupted by the disorder of $\text{IrO}_6/\text{RhO}_6$ octahedral rotations⁹, our measurements of the superlattice Bragg peaks associated with these rotations (Section III.E) reveal no significant change in correlation lengths at x_c . Other doping-induced structural changes, such as a sudden jump in Ir-O-Ir bond angle, have previously been reported in the vicinity of x_c [Ref. 9]. However, these structural changes appear to be discontinuous, while the observed decrease in T_{N1} and T_{N2} is clearly continuous.

An alternative explanation is provided by percolation theory (Figs. 4(b,c)), which has proven extremely successful at describing magnetism in doped cuprates such as $\text{La}_2\text{Cu}_{1-x}(\text{Zn,Mg})_x\text{O}_4$ [Ref. 38]. This argument as-

sumes that $\text{Sr}_2\text{Ir}_{1-x}\text{Rh}_x\text{O}_4$ can be adequately described by a local moment picture for $x \leq 0.24$, a claim which appears reasonably well-justified based on previous resistivity data⁹. As Sr_2IrO_4 is effectively a two-dimensional $S = 1/2$ Heisenberg antiferromagnet, we expect the conventional (i.e. spin-only) percolation threshold for this system to be $x_p = 0.407$ [Ref. 39]. Since each Rh^{3+} dopant ion introduces two non-magnetic vacancies, the effective site dilution, x_c^{eff} , will be equal to twice the nominal Rh concentration. We suggest that the apparent discrepancy between $x_c^{eff} = 2x_c = 0.34$ and $x_p = 0.407$ may reflect novel percolation behavior arising from strong SOC effects. Recent theoretical work^{40,41} has shown that quantum orbital systems are much more sensitive to site dilution than pure spin systems, and can display considerably lower percolation thresholds. In a system where the spin and orbital degrees of freedom are strongly entangled, as in Sr_2IrO_4 , it is therefore unsurprising that a spin-only percolation calculation overestimates the value of x_p . This result suggests a full theoretical description of dilute magnetism in $\text{Sr}_2\text{Ir}_{1-x}\text{Rh}_x\text{O}_4$ must account for both spin and orbital percolation effects, raising the possibility of exciting new percolation physics in the strong SOC regime.

In conclusion, we have used a combination of resonant x-ray techniques to investigate the chemical, electronic, and magnetic properties of the doped spin-orbital Mott insulator $\text{Sr}_2\text{Ir}_{1-x}\text{Rh}_x\text{O}_4$. XAS measurements clearly demonstrate that Rh-doping introduces Rh^{3+} and Ir^{5+} ions into this material, leading to (1) hole-doping and (2) magnetic dilution of the system. RMXS measurements reveal a doping-induced change in magnetic structure at $x \leq 0.07$, which leads to the development of a canted ab -plane antiferromagnetic state (AF-II) for $x = 0.07, 0.11$, and 0.15 . Magnetic order is fully suppressed above $x_c \sim 0.17$ (or $x_c^{eff} \sim 0.34$), a result which suggests novel percolation effects and intriguing differences from diluted cuprates. We hope these results will help to motivate further theoretical and experimental work on $\text{Sr}_2\text{Ir}_{1-x}\text{Rh}_x\text{O}_4$ and other doped 5d systems in the future.

Acknowledgments

The authors would like to acknowledge valuable discussions with Y. Cao, D. Dessau, D. Haskel, and J.W. Kim. Work at the University of Toronto was supported by NSERC of Canada, the Banting Postdoctoral Fellowship program, and the Canada Research Chair program. Work at the University of Kentucky was supported by NSF through grants DMR-0856234, DMR-1265162, and EPS-0814194. Use of SXRMB at the Canadian Light Source is supported by NSERC of Canada, NRC of Canada, CIHR, and the University of Saskatchewan. Use of the Advanced Photon Source at Argonne National

Laboratory and the National Synchrotron Light Source at Brookhaven National Laboratory is supported by the U.S. Department of Energy, Office of Science, Office of

Basic Energy Sciences, under Contract Nos. DE-AC02-06CH11357 and DE-AC02-98CH10886.

-
- ¹ B.J. Kim, H. Jin, S.J. Moon, J.-Y. Kim, B.-G. Park, C.S. Leem, J. Yu, T.W. Noh, C. Kim, S.-J. Oh, J.-H. Park, V. Durairaj, G. Cao, and E. Rotenberg, Phys. Rev. Lett. **101**, 076402 (2008).
 - ² B.J. Kim, H. Ohsumi, T. Komesu, S. Sakai, T. Morita, H. Takagi, and T. Arima, Science **323**, 1329 (2009).
 - ³ G. Jackeli and G. Khaliullin, Phys. Rev. Lett. **102**, 017205 (2009).
 - ⁴ J.H. Kim, D. Casa, M.H. Upton, T. Gog, Y.-J. Kim, J.F. Mitchell, M. van Veenendaal, M. Daghofer, J. van den Brink, G. Khaliullin, and B.J. Kim, Phys. Rev. Lett. **108**, 177003 (2012).
 - ⁵ M.K. Crawford, M.A. Subramanian, R.L. Harlow, J.A. Fernandez-Baca, Z.R. Wang, and D.C. Johnston, Phys. Rev. B **49**, 9198 (1994).
 - ⁶ Q. Huang, J.L. Soubeyroux, O. Chmaisnen, I. Natali Sora, A. Santoro, R.J. Cava, J.J. Krajewski, and W.F. Peck, Jr., J. Solid State Chem. **112**, 355 (1994).
 - ⁷ F. Wang and T. Senthil, Phys. Rev. Lett. **106**, 136402 (2011).
 - ⁸ H. Watanabe, T. Shirakawa, and S. Yunoki, Phys. Rev. Lett. **110**, 027002 (2013).
 - ⁹ T.F. Qi, O.B. Korneta, L. Li, K. Butrouna, V.S. Cao, X. Wan, P. Schlottmann, R.K. Kaul, and G. Cao, Phys. Rev. B **86**, 125105 (2012).
 - ¹⁰ J.S. Lee, Y. Krockenberger, K.S. Takahashi, M. Kawasaki, and Y. Tokura, Phys. Rev. B **85**, 035101 (2012).
 - ¹¹ Y. Klein and I. Terasaki, J. Phys.: Condens. Matter **20**, 295201 (2008).
 - ¹² Y. Klein and I. Terasaki, J. Electron. Mater. **38**, 1331 (2009).
 - ¹³ Y. Cao, Bull. Amer. Phys. Soc. **58**, C1.4 (2013); <http://meetings.aps.org/link/BAPS.2013.MAR.C1.4>.
 - ¹⁴ S. Calder, G.-X. Cao, M.D. Lumsden, J.W. Kim, Z. Gai, B.C. Sales, D. Mandrus, and A.D. Christianson, Phys. Rev. B **86**, 220403 (2012).
 - ¹⁵ S.A. Carter, B. Batlogg, R.J. Cava, J.J. Krajewski, W.F. Peck, Jr., and L.W. Rupp, Jr., Phys. Rev. B **51**, 17184 (1995).
 - ¹⁶ R.J. Cava, B. Batlogg, K. Kiyono, H. Takagi, J.J. Krajewski, W.F. Peck, Jr., L.W. Rupp, Jr., and C.H. Chen, Phys. Rev. B **49**, 11890 (1994).
 - ¹⁷ A.J. Gatumu, R. Berthelot, S. Muir, A.W. Sleight, and M.A. Subramanian, J. Solid State Chem. **190**, 257 (2012).
 - ¹⁸ M. Ge, T.F. Qi, O.B. Korneta, D.E. De Long, P. Schlottmann, W.P. Crummett, and G. Cao, Phys. Rev. B **84**, 100402 (2011).
 - ¹⁹ O.B. Korneta, T.F. Qi, S. Chikara, S. Parkin, L.E. De Long, P. Schlottmann, and G. Cao, Phys. Rev. B **82**, 115117 (2010).
 - ²⁰ T. Shimura, Y. Inaguma, T. Nakamura, M. Itoh, and Y. Morii, Phys. Rev. B **52**, 9143 (1995).
 - ²¹ M. Itoh, T. Shimura, Y. Inaguma, and Y. Morii, J. Solid State Chem. **118**, 206 (1995).
 - ²² R.S. Perry, F. Baumberger, L. Balicas, N. Kikugawa, N.J.C. Ingle, A. Rost, J.F. Mercure, Y. Maeno, Z.X. Shen, and A.P. Mackenzie, New J. Phys. **8**, 175 (2006).
 - ²³ C. Martins, M. Aichhorn, L. Vaugier, and S. Biermann, Phys. Rev. Lett. **107**, 266404 (2011).
 - ²⁴ G. Cao, J. Bolivar, S. McCall, J.E. Crow, and R.P. Guertin, Phys. Rev. B **57**, R11039 (1998).
 - ²⁵ K. Hamalainen, D.P. Siddons, J.B. Hastings, and L.E. Berman, Phys. Rev. Lett. **67**, 2850 (1991).
 - ²⁶ F.M.F. de Groot, M.H. Krisch and J. Vogel, Phys. Rev. B **66**, 195112 (2002).
 - ²⁷ J.P. Hill and D.F. McMorrow, Acta Cryst. **A52**, 236 (1996).
 - ²⁸ J.C. Fuggle and J.E. Inglesfeld, *Unoccupied Electronic States: Fundamentals for XANES, EELS, IPS, and BIS* (Springer-Verlag, New York, 1992).
 - ²⁹ F. Ye, S. Chi, B.C. Chakoumakos, J.A. Fernandez-Baca, T.F. Qi, and G. Cao, Phys. Rev. B **87**, 140406(R) (2013).
 - ³⁰ A.S. Wills, Physica B **276**, 680 (2000).
 - ³¹ O. Bunau and Y. Joly, J. Phys.: Condens. Matter **21**, 345501 (2009).
 - ³² S. Boseggia, R. Springell, H.C. Walker, A.T. Boothroyd, D. Prabhakaran, D. Wermeille, L. Bouchenoire, S.P. Collins, and D.F. McMorrow, Phys. Rev. B **85**, 184432 (2012).
 - ³³ J.W. Kim, Y. Choi, J. Kim, J.F. Mitchell, G. Jackeli, M. Daghofer, J. van den Brink, G. Khaliullin, and B.J. Kim, Phys. Rev. Lett. **109**, 037204 (2012).
 - ³⁴ S. Boseggia, R. Springell, H.C. Walker, H.M. Ronnow, Ch. Ruegg, H. Okabe, M. Isobe, R.S. Perry, S.P. Collins, and D.F. McMorrow, Phys. Rev. Lett. **110**, 117207 (2013).
 - ³⁵ K. Ohgushi, J. Yamaura, H. Ohsumi, K. Sugimoto, S. Takeshita, A. Tokuda, H. Takagi, M. Takata, and T. Arima, Phys. Rev. Lett. **110**, 217212 (2013).
 - ³⁶ L.C. Chapon and S.W. Lovesey, J. Phys.: Condens. Matter **23**, 252201 (2011).
 - ³⁷ M. Moretti Sala, S. Boseggia, D.F. McMorrow, and G. Monaco, arXiv:1308.0128v1 (2013).
 - ³⁸ O.P. Vajk, P.K. Mang, M. Greven, P.M. Gehring, and J.W. Lynn, Science **295**, 1691 (2002).
 - ³⁹ D. Stauffer and A. Aharony, *Introduction to Percolation Theory, Revised 2nd Ed.* (Taylor and Francis, Bristol, PA, 1994).
 - ⁴⁰ T. Tanaka and S. Ishihara, Phys. Rev. Lett. **98**, 256402 (2007).
 - ⁴¹ T. Tanaka and S. Ishihara, Phys. Rev. B **79**, 035109 (2009).